CHAPTER 3

2D MoS_2/$MnIn_2S_4$ hetero-interface with improved interfacial charge carrier transfer for photocatalytic H_2O_2 production

3.1 INTRODUCTION

In recent decades, a wide range of photocatalysts have been explored for H_2O_2 production. Notable examples include titanium dioxide (TiO_2)-based photocatalysts [11], carbon nitride (g-C_3N_4)-based photocatalysts [91,92], transition metal complexes [93], transition metal sulfides [36,94], and bismuth (Bi)-containing semiconductors [95]. Among these, metal sulfides have attracted significant interest in photocatalysis due to their tunable band gaps, favorable electronic structures, and abundant active sites [96].

In this context, MoS_2, a typical layered transition metal dichalcogenide, has attracted significant attention due to its low cost, large surface area, strong visible light response, tunable bandgap structure, and favorable photocatalytic performance [97,98]. In particular, exfoliated or few-layered MoS_2 nanosheets with a 2D structure have emerged as promising photocatalysts. The unique optical and electronic properties of 2D MoS_2 contribute to better photoresponse and charge separation in photocatalysts [99]. As the number of layers decreases, MoS_2 exhibits enhanced properties that improve its photocatalytic performance [100,101]. To date, several studies have reported significant enhancements in photocatalytic activity using few-layer MoS_2 heterojunction composites, including In_2S_3/MoS_2 [102], CdS/MoS_2 [103], MoS_2/rGO/CdS [104], WS_2-MoS_2 [105], MoS_2/g-C_3N_4 [106], and $MoS_2/Mn_{0.2}Cd_{0.8}S$ [107]. These heterostructured photocatalysts, which couple 2D MoS_2 with other semiconductors, facilitate enhanced separation of photogenerated charge carriers and broaden solar light absorption. Composite formation effectively suppresses the recombination of charge carriers, thereby improving overall photocatalytic efficiency.

On the other hand, ternary chalcogenide AB_2X_4 semiconductors have recently been recognized for their significant potential as visible-light-active photocatalysts, owing to their tunable optical properties, unique electronic structure, narrow band gaps, and chemical photostability [108,109]. Among them, $MnIn_2S_4$ stands out as an ideal photocatalyst due to its appropriate band gap for visible light absorption and the high reduction potential of its conduction band electrons. Chen et al. recently developed 2D/2D g-$C_3N_4/MnIn_2S_4$ Z-scheme heterostructured photocatalysts for H_2 production and antibiotic degradation. Their study showed that heterostructure formation significantly enhanced visible light absorption and promoted efficient interfacial charge separation, resulting in superior photocatalytic performance compared to pristine g-C_3N_4 and $MnIn_2S_4$ [110]. Similarly, Song et al. fabricated $Cu_7S_4/MnIn_2S_4$ semiconductor heterostructures using a simple oil bath and hydrothermal method. The nanocomposite, featuring ultra-thin 2D nanosheets and Cu_7S_4 nanoparticles uniformly distributed on $MnIn_2S_4$, exhibited a photocatalytic hydrogen evolution rate of 13.81 μmol h^{-1}, nearly 18 times higher than pure $MnIn_2S_4$. The enhanced performance was attributed to the forming of a p-n heterojunction that suppressed electron-hole recombination [111]. Deng et al. designed and constructed a $MnIn_2S_4/WO_3$ (Yb, Tm) photocatalytic system, incorporating a Z-scheme heterojunction to regulate spatial charge separation and improve light absorption through Yb^{3+} and Tm^{3+} doping. The system was evaluated for H_2O_2 production, showing remarkable activity, producing 37.2 and 8.8 times more H_2O_2 than WO_3 and $MnIn_2S_4$, respectively [112]. However, there are no prior reports on the development of a 2D/2D $MoS_2/MnIn_2S_4$ heterostructure photocatalyst.

In the current study, a heterostructure was constructed by combining few-layered MoS_2 with $MnIn_2S_4$, effectively integrating the advantages of both materials. This combination exhibits strong visible-light absorption, a low recombination rate of photoinduced electron-hole pairs, and excellent photocatalytic activity. Herein, we design and develop a novel 2D $MoS_2/MnIn_2S_4$ heterostructure photocatalyst through a green hydrothermal process. The small petals of $MnIn_2S_4$ were embedded on ultrathin 2D MoS_2 nanosheets, forming a well-integrated heterostructure (Scheme 3.1). The 2D morphology of $MnIn_2S_4$ and MoS_2 enhances interfacial contact and facilitates efficient charge transfer between the two components. Various characterization techniques, including X-ray diffractometer (XRD), scanning electron microscope (SEM), transmission electron microscope (TEM), diffuse reflectance spectroscopy (DRS), photoluminescence (PL), contact angle, and electrochemical measurements, were employed to investigate the intrinsic relationship between the 2D hetero-interface structure and the significantly enhanced photocatalytic activity of the $MoS_2/MnIn_2S_4$ heterostructure. The photocatalytic activities of the resulting samples were assessed for H_2O_2 production. The improved photocatalytic performance of the heterostructure systems can primarily be attributed to the Z-scheme mechanism. This mechanism effectively harnesses the strong reduction capability of photo-generated electrons in the conduction band of $MnIn_2S_4$ nanosheets and the high oxidation capability of photo-generated holes in the valence band of 2D MoS_2 nanosheets. Furthermore, the mechanism of the H_2O_2 production process has been thoroughly investigated. The pathway is elucidated through scavenger studies, and the reactive species involved in the photocatalytic H_2O_2 production are identified based on confirmatory tests. This research will guide the future design of more versatile Z-scheme sulfide/chalcogenide heterostructure composites for H_2O_2 production.

3.2 EXPERIMENTAL SECTION

3.2.1 Preparation of 2D MoS_2 nanosheets

Pristine MoS_2 nanosheets were prepared through a one-step hydrothermal treatment[113]. Typically, one mmol of $(NH_4)_6Mo_7O_{24}\cdot 4H_2O$ and 30 mmol of NH_2CSNH_2

were dissolved in 35 ml of deionized water under vigorous stirring to form a homogeneous solution. The resulting mixture was then transferred to a 50 ml Teflon-lined autoclave and maintained at 210°C for 24 hours. After the reaction, the precipitates were allowed to cool naturally to room temperature, washed multiple times with water and absolute ethanol, and collected by ultracentrifugation at 25,000 rpm. The final products were dried at 60°C in a vacuum oven and stored for further use.

For the preparation of 2D MoS_2 nanosheets, 150 mg of the synthesized MoS_2 powder was initially dispersed in 80 mL of a mixed solvent of N-methyl pyrrolidone (NMP) and deionized water (50/50 (vol%)) in a stoppered conical flask[100]. The flask was then subjected to ultrasonic bath sonication for 120 minutes. The resulting suspension was left overnight, and the dispersion of exfoliated MoS_2 was isolated. Finally, the exfoliated MoS_2 was centrifuged at 25,000 rpm for 25 minutes, and the exfoliated MoS_2 powder was collected for further use.

3.2.2 Preparation of $MnIn_2S_4$

Firstly, 0.198 g of Manganese chloride tetrahydrate (1 mmol) and 0.537g of indium chloride tetrahydrate (2 mmol) were dissolved in 35 ml of deionized water under vigorous stirring for one hour. Then, 0.381g of thiourea (5 mmol) was added to the solution and stirred for two more hours. The suspension was transferred to a Teflon-lined stainless steel autoclave and heated at 210°C for 24 hours. Once the reaction was complete, the samples were allowed to cool naturally to room temperature, washed with ethanol, and dried in a vacuum oven [110].

3.2.3 Synthesis of 2D $MoS_2/MnIn_2S_4$

The 2D $MoS_2/MnIn_2S_4$ heterostructures with varying concentrations of $MnIn_2S_4$ nanosheets were synthesized using a straightforward hydrothermal method. Initially, a certain amount of 2D MoS_2 nanosheets was dispersed in deionized water and subjected to ultrasonication for 60 minutes to form a uniform suspension. Next, manganese chloride tetrahydrate (1 mmol), indium chloride tetrahydrate (2 mmol), and thiourea (5 mmol) were dissolved in deionized water with constant stirring on a magnetic stirrer. After one hour of stirring, the 2D MoS_2 suspension was added to the mixture and stirred for two more hours. The resulting mixture was then transferred to a Teflon-lined autoclave and heated at 210 °C for 24 hours. Once the reaction was complete, the samples were allowed to cool naturally to room temperature, then washed multiple times with water and ethanol and collected by centrifugation. The process produced 2D $MoS_2/MnIn_2S_4$ nanocomposites with varying $MnIn_2S_4$ weight ratios, designated as MS/MnIS-x, where x corresponds to 10, 20, 40, 60, and 80, representing the weight percent of $MnIn_2S_4$ relative to 2D MoS_2 in the reaction system.

3.2.4 Photocatalytic H_2O_2 production

The photocatalytic H_2O_2 production experiment was carried out by dispersing 5 mg of the synthesized photocatalyst powder in 20 mL of a deionized water/ethanol mixture (95:5 vol%). The dispersion was facilitated through 10 minutes of ultrasonic bath treatment. Afterward, oxygen was bubbled through the solution and kept in the dark for 30 minutes to ensure equilibrium. The suspension was then exposed to irradiation from a solar simulator. Following one hour of photocatalytic reaction, a 2 mL aliquot was extracted, and the photocatalyst was separated from the reaction solution.

The concentration of H_2O_2 was quantified using the iodometric method [86,114,115]. To the 2 mL aliquot (post photocatalyst removal), 2 mL of 0.1 M KI and 50 μL of 0.01M ($(NH_4)_6Mo_7O_{24}\cdot4H_2O$) were added and thoroughly mixed. The reaction mixture was kept in the dark for 20 minutes to allow for a complete reaction. In this process, KI is oxidized by H_2O_2, releasing I_2, which then reacts with excess I^- (from KI) to form the yellow-colored triiodide anion (I_3^-) through the reaction: $H_2O_2 + 3I^- + 2H^+ \rightarrow I_3^-$. The amount of I_3^- generated is directly proportional to the concentration of H_2O_2 in the sample. Finally, the absorbance of the resulting solution was measured using UV–vis spectroscopy, showing a characteristic intense absorption peak around 352 nm.

Furthermore, to achieve optimal yields in H_2O_2 production, the experimental conditions, including pH, were systematically optimized. The primary reactive species generated during the photocatalytic process were identified using trapping experiments under irradiation. The contributions of electrons (e^-), superoxide radicals ($\bullet O_2^-$), and holes (h^+) to H_2O_2 production were assessed by introducing $AgNO_3$, p-BQ, and EDTA-2Na as scavengers.

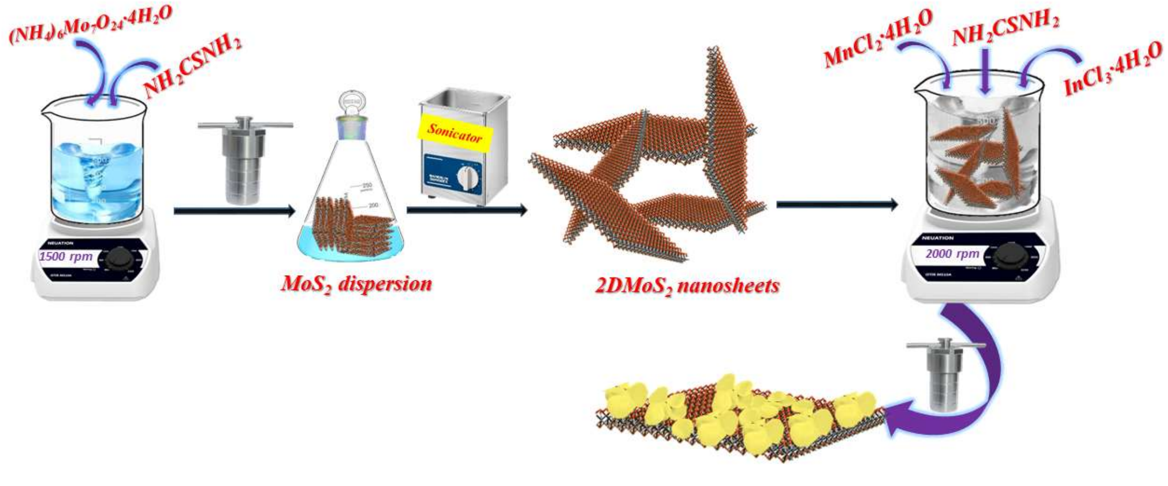

Scheme 3.1 Schematic diagram illustrating the synthesis process of as-designed MS/MnIS-*x* heterostructure photocatalysts.

3.3 RESULTS AND DISCUSSION

Powder XRD was carried out to investigate the phase purity and crystal structures of the 2D MoS_2, $MnIn_2S_4$, and MS/MnIS-*x* heterostructures. Figure 3.1 shows the corresponding XRD patterns of the various samples. The XRD pattern traced in purple is of the as-prepared 2D MoS_2 nanosheets. The observed diffraction peaks at two theta (2θ) values of 14.2°, 33.4°, and 58.8° can be uniquely attributed to the (002), (100), and (110) crystal planes of standard hexagonal MoS_2 (2H MoS_2, JCPDS card No. 731508), respectively, revealing the high purity of the sample. There is an apparent broadening of all the peaks in the diffraction patterns, which suggests the nanoscales of the crystallites in different dimensions [113]. The red trace represents the diffraction pattern of the standard cubic structure $MnIn_2S_4$ phase (JCPDS No. 85-1229). The characteristic peaks of MoS_2 at (002) and (110) were observed in all 2D $MoS_2/MnIn_2S_4$ heterostructures, confirming that the composite structure consists of hexagonal MoS_2 and cubic $MnIn_2S_4$. No diffraction peaks associated with impurities were detected, confirming the high purity of the synthesized heterostructure photocatalysts.

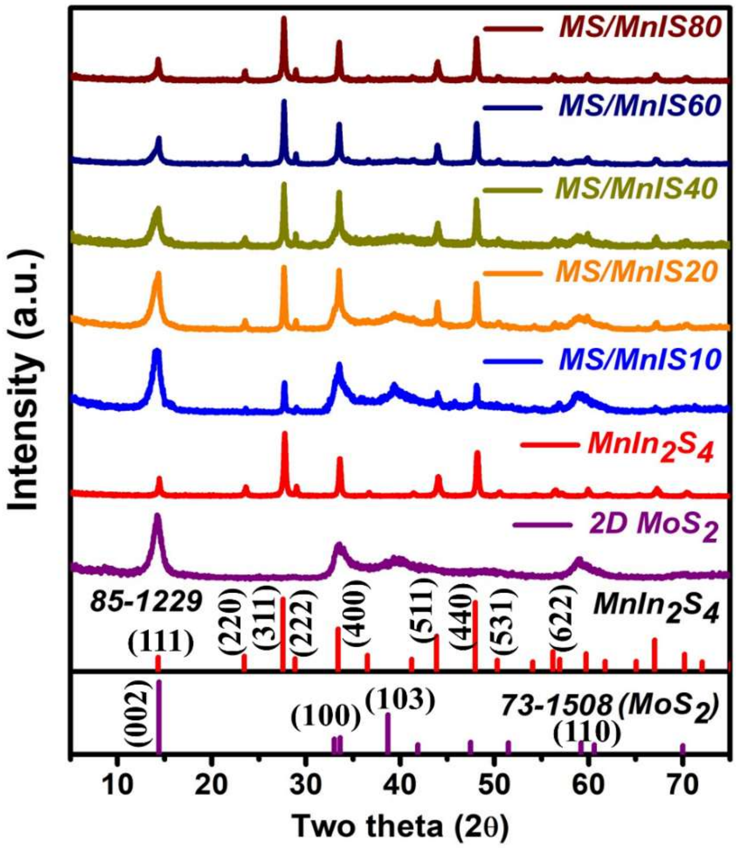

Figure 3.1. XRD patterns of 2D MoS_2, $MnIn_2S_4$, and MS/MnIS-*x* heterostructure photocatalysts.

The optical properties of the 2D MoS_2 nanosheets, produced via liquid-phase ultra-sonication, were examined using UV-visible absorbance spectrophotometry. A slight shift in the UV-visible spectral peak toward a lower wavelength (Figure 3.2a) suggests a change in the bandgap due to exfoliation. Additionally, the light absorbance in the visible region was significantly enhanced after exfoliation compared to bulk MoS_2. Figure 3.2a (inset picture) indicates the successful and stable dispersion of exfoliated MoS_2 nanosheets.

Similarly, the optical characteristics of 2D MoS_2, $MnIn_2S_4$, and the MS/MnIS-*x* heterostructure were explored through solid-state UV–Vis NIR analysis, as shown in Figure 3.2b. From the absorbance spectra, it is clear that 2D MoS_2 shows a strong visible light absorption band at a range of 300-1350 nm. Similarly, pristine $MnIn_2S_4$ exhibited visible light absorption with a characteristic absorption edge near 680 nm. Compared to pristine $MnIn_2S_4$, the formation of the MS/MnIS-*x* heterostructure resulted in a significant redshift of the absorption edge, with strong absorption observed in the visible to NIR range from approximately 340 to 1350 nm. The DRS results demonstrated that the formation of 2D $MoS_2/MnIn_2S_4$ heterostructures allows for more efficient exploitation of solar energy. Further, the band gap energy (E_g) of the 2D MoS_2, $MnIn_2S_4$, was calculated by the Tauc plot method using Equation 3.1.

$$(\alpha h v)^{\frac{1}{n}} = A(hv - E_g) \ldots\ldots\ldots\ldots\ldots (3.1)$$

Here hv, and α represent the photoelectron energy, and absorption coefficient, respectively. The measured band gap energies of 2D MoS_2 and $MnIn_2S_4$ were 1.52 eV and 1.88 eV, respectively, as shown in Figure 3.2d and 3.2e. The calculated band gap of bulk MoS_2 (before exfoliation) are shown in Figure 3.2c. These results indicate that, after successful exfoliation into nanosheets, the band gap energy increased from 1.31 eV to 1.52 eV.

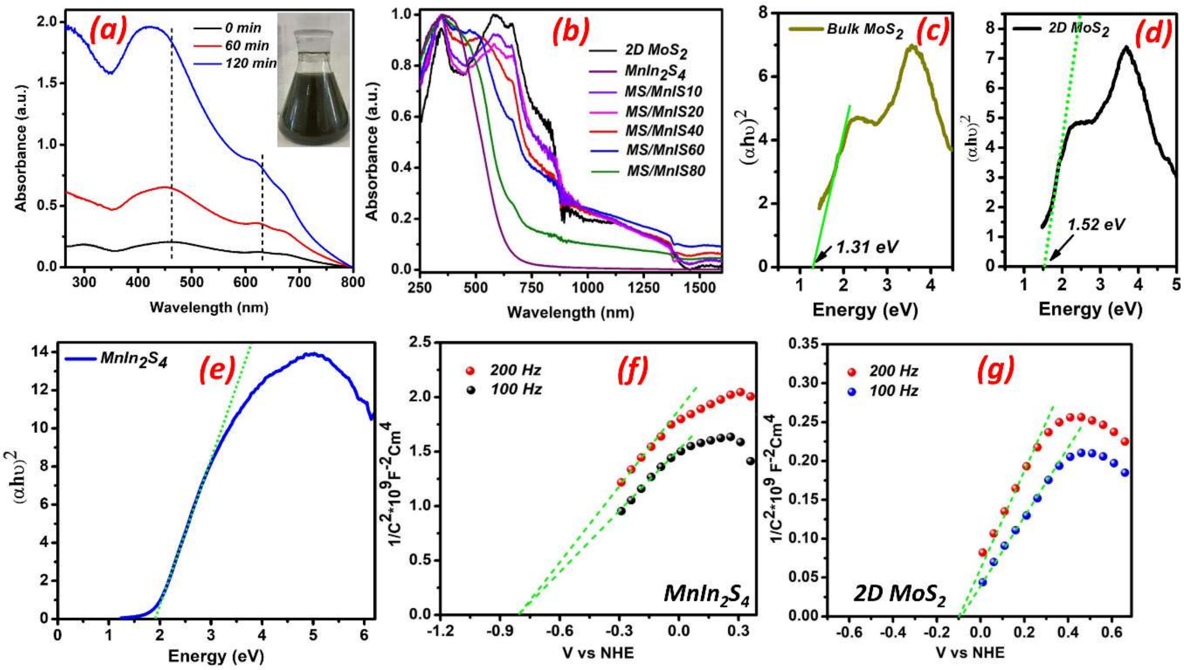

Figure. 3.2. (a) UV visible absorbance spectra of bulk MoS_2 and exfoliated MoS_2 nanosheets and inset Images of exfoliated MoS_2 nanosheets were captured 24 hours after ultrasonication bath treatment, confirming stable dispersion **(b)** Solid-state UV-DRS absorbance spectra of 2D MoS_2, $MnIn_2S_4$, and MS/MnIS-*x* heterostructure photocatalysts **(c)** Tauc plot of bulk MoS_2 (un-exfoliated) **(d, e)** Tauc plot of 2D MoS_2 and $MnIn_2S_4$. Mott-Schottky plot of **(f)** $MnIn_2S_4$ and **(g)** 2D MoS_2.

Mott-Schottky (MS) measurements were carried out at 100 Hz and 200 Hz to investigate the band structure and semiconductor type. Figure 3.2 (f and g) shows the MS curves for 2D MoS_2 and $MnIn_2S_4$ samples. Both 2D MoS_2 and $MnIn_2S_4$ exhibited positive MS slopes, confirming their *n*-type semiconductor characteristics. The conduction band potentials were determined to be -0.1 V for 2D MoS_2 and -0.81 V for $MnIn_2S_4$ versus NHE by fitting the $1/C^2$ vs. potential plot. By combining the MS results with the energy band gaps of 2D MoS_2 and $MnIn_2S_4$, as determined by the Tauc plot, the valence band positions were calculated to be 1.42 V for 2D MoS_2 and 1.07 V for $MnIn_2S_4$, respectively, using the formula $E_{VB} = E_{CB} + Eg$ [29,116]. Here, E_{VB} represents the valence band edge position, and E_{CB} denotes the conduction band edge position. It is noteworthy that the CB potentials of $MnIn_2S_4$ are more negative than the reduction potential of $O_2/{\bullet}O_2^-$ (−0.33 V vs. NHE) and O_2/H_2O_2 (0.68 V vs. NHE). This indicates that their reduction potential is sufficient to drive the formation of H_2O_2.

The morphologies and microstructures of $MnIn_2S_4$, 2D MoS_2, and the MS/MnIS40 heterostructures were thoroughly characterized using SEM and TEM. The analysis revealed that both 2D MoS_2 and $MnIn_2S_4$ exhibit a layered structure with lateral dimensions of several hundred nanometers, respectively. Figure 3.3 presents the SEM images of $MnIn_2S_4$ and the MS/MnIS40. The pure $MnIn_2S_4$ exhibits a distinctive nanoflower-like structure composed of small petal-like features, as shown in Figures 3.3a and 3.3b. Notably, these petal-like formations gradually orient themselves into a cohesive nanoflower morphology. This unique morphology is advantageous for photocatalytic H_2O_2 production, as it provides many active sites for the reaction. Similarly, the SEM images of the MS/MnIS40 heterostructure (Figure 3.3c, d) illustrate the formation of small petal-like nanostructures of $MnIn_2S_4$ embedded on the thin, layered 2D MoS_2 nanosheets. The corresponding SEM elemental mapping images confirm the uniform distribution of Mn, In, Mo, and S elements within the MS/MnIS40 heterostructure, indicating partial coverage of the 2D MoS_2 surface by $MnIn_2S_4$. However, as the $MnIn_2S_4$ loading increases, excessive deposition leads to agglomeration, resulting in the formation of nanoflowers that entirely cover the 2D MoS_2 surface. Additionally, Figure 3.4 (a, b) presents the SEM images and elemental mapping for the MS/MnIS60 and MS/MnIS80 samples. No extra elements are detected in these samples, confirming the high purity and successful formation of the heterostructure in the synthesized materials.

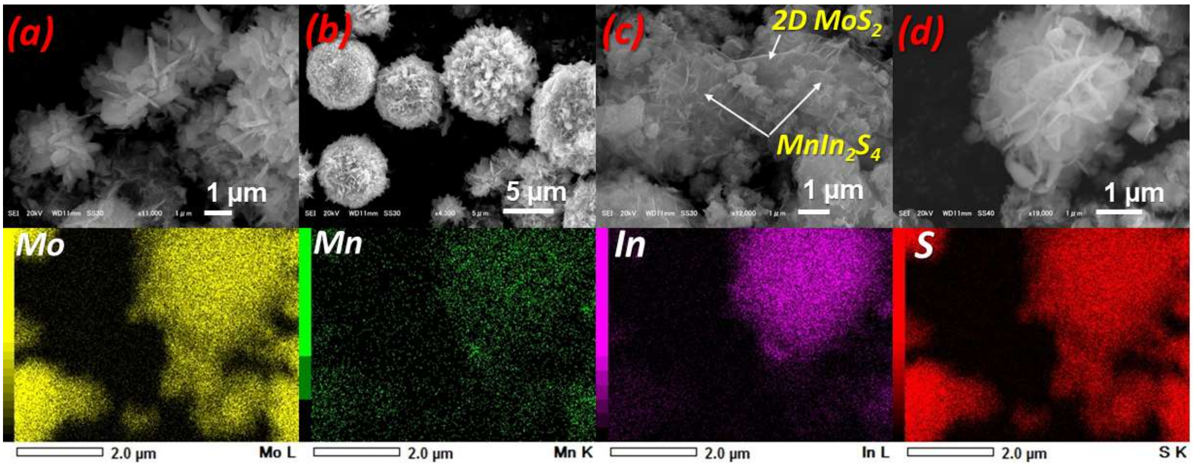

Figure 3.3. **(a, b)** SEM images of pristine $MnIn_2S_4$ **(c)** SEM images of MS/MnIS40 heterostructure photocatalysts **(d)** SEM image with corresponding elemental maps (Mo, Mn, In, S) of MS/MnIS40 heterostructure photocatalysts.

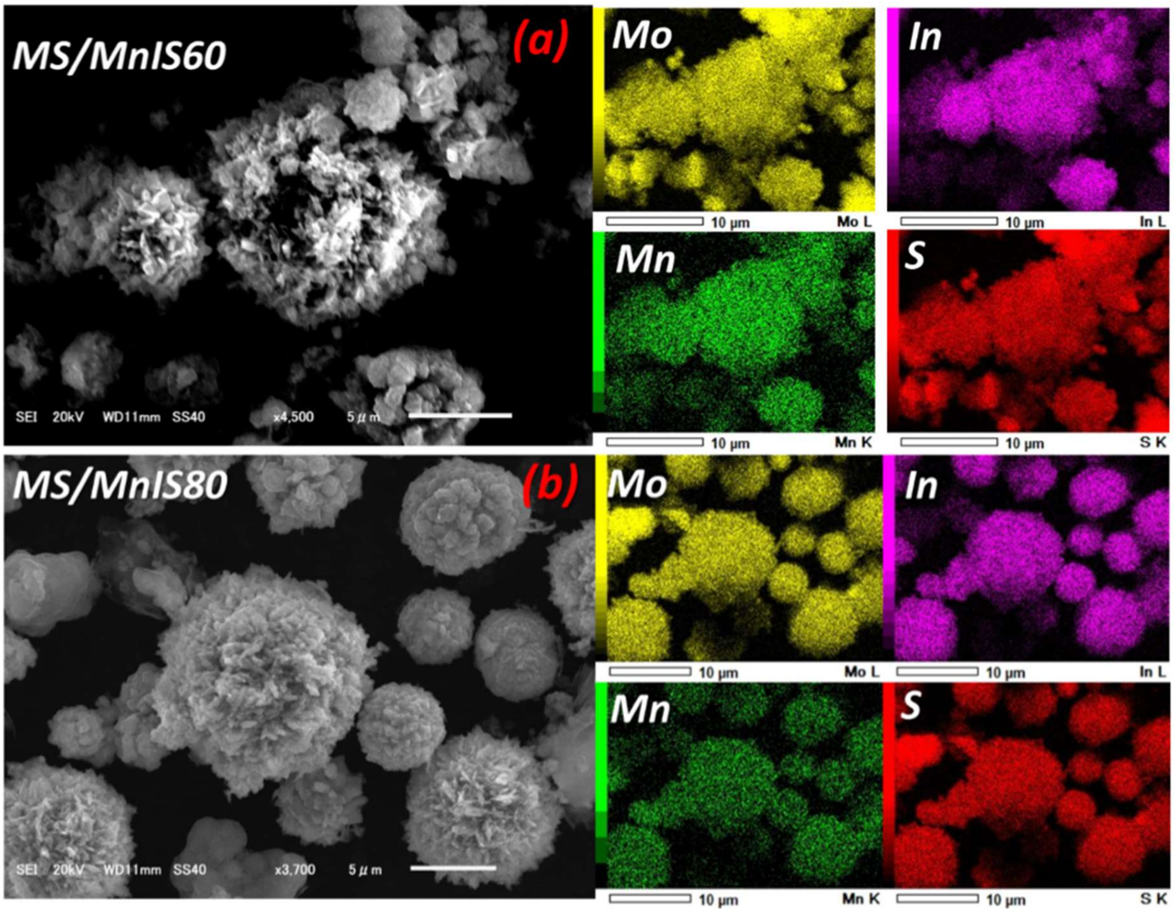

Figure 3.4. (a, b) SEM images and elemental mapping of MS/MnIS60 and MS/MnIS80 heterostructure photocatalysts.

To further confirm the morphology and structure of 2D MoS_2, $MnIn_2S_4$, and the MS/MnIS40 heterostructure were observed using TEM and high-resolution TEM (HRTEM). Notably, the TEM images of the $MnIn_2S_4$ (Figure 3.5a) and 2D MoS_2 (Figure 3.5d) display layered structures with a nearly transparent appearance, consistent with the presence of ultrathin nanosheets. The inverse fast Fourier transform (IFFT) images and spectra of the HRTEM images of pristine $MnIn_2S_4$, as shown in Figure 3.5c, reveal distinct lattice fringes of 0.32 nm, corresponding to the (311) crystal plane of $MnIn_2S_4$, which is consistent with the intense peak observed in the XRD pattern (JCPDS No. 85-1229). Figure 3.5d reveals that the 2D MoS_2 consists of few-layered, curled nanosheets with a scattered orientation. As shown in Figure 3.5e, the interlayer spacing of 6.3 Å corresponds to the (002) planes of MoS_2, verifying its hexagonal (2H) structure. These nanosheets exhibit higher crystallinity and a relatively intact layered configuration, which aligns well with the XRD results. The HRTEM images of the 2D MoS_2 nanosheets in Figure 3.5e reveal structural defects in the 2H MoS_2, typically characterized by cracks and misaligned basal planes, as previously reported in the literature [113,117]. After forming the 2D MoS_2 and $MnIn_2S_4$ heterostructures (MS/MnIS40), the structure exhibits an ultrathin nanosheet-on-nanosheet morphology (Figure 3.5 (f, g)) with a large contact surface. The IFFT images and spectra derived from the HRTEM image of the 2D/2D heterostructure (Figure 3.5h) reveal lattice fringes of $MnIn_2S_4$ (0.32 nm) and 2D MoS_2 (0.63 nm), confirming strong interfacial contact between the two materials and the successful formation of the heterostructure. This extensive, intimate interface enables multiple pathways for carrier migration, enhancing charge separation efficiency. Furthermore, the elemental mapping analysis of the selected region in Figure 3.5i for the MS/MnIS40 heterostructure demonstrates the well-defined spatial distribution of Mo, Mn, In, and S (Figure 3.5i). The electron microscopy results reveal a uniform and intimate coupling within the 2D structure of MoS_2/$MnIn_2S_4$, which substantially increases the contact area. This expanded interface improves the separation of photoinduced charge carriers and facilitates more efficient electron transfer within the heterostructure, significantly enhancing photocatalytic activity [118].

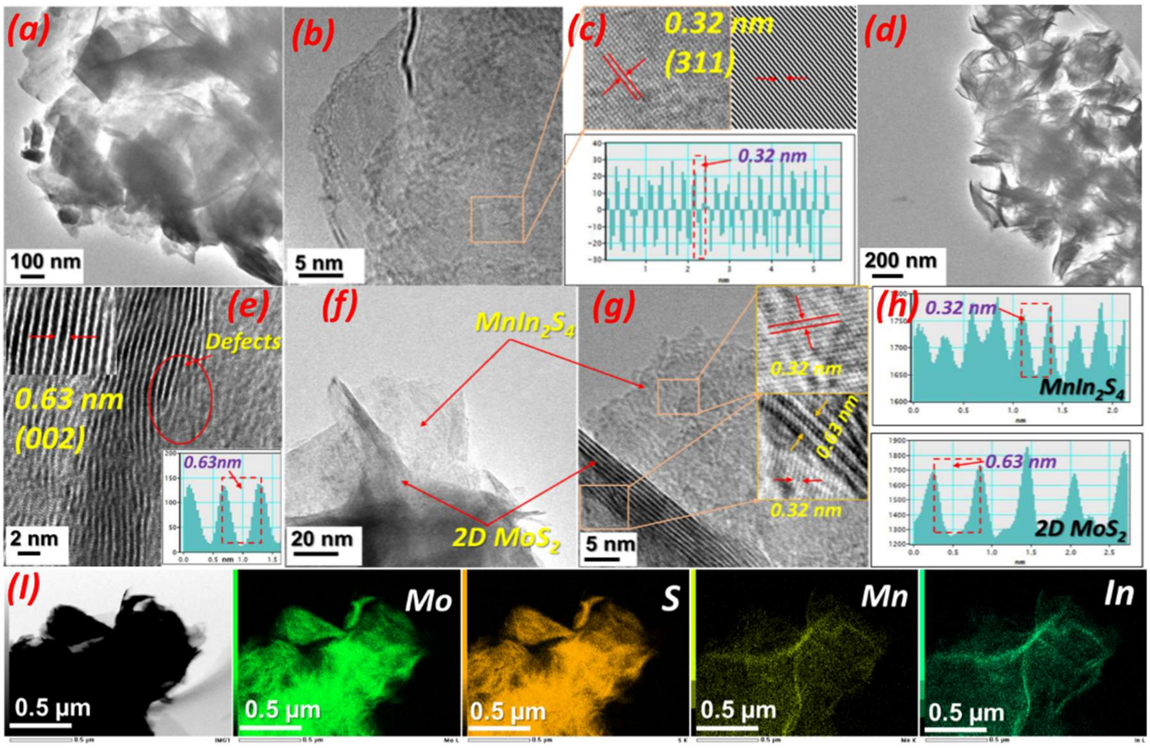

Figure 3.5. TEM, HR-TEM, and IFFT images of **(a, b, and c)** pure $MnIn_2S_4$ **(d, e)** 2D MoS_2 **(f, g, and h)** MS/MnIS40 heterostructure. **(I)** STEM elemental mapping of MS/MnIS40 heterostructure photocatalysts.

The X-ray photoelectron spectroscopy (XPS) analysis revealed the chemical states and interfacial interactions in the 2D MoS_2, $MnIn_2S_4$, and MS/MnIS40 samples. The HR-XPS data was calibrated using the C 1s 284.8 eV binding energy [119]. The XPS survey spectrum in Figure 3.6a confirms the presence of Mo and S elements in MoS_2 and Mn, In, and S elements in $MnIn_2S_4$. Similarly, the survey spectrum of the MS/MnIS40 samples shows Mo, Mn, In, and S, further indicating the successful formation of heterostructures of 2D MoS_2 and $MnIn_2S_4$. The high resolution (HR) Mn 2p spectra of $MnIn_2S_4$ (Figure 3.6b) show characteristic peaks at binding energies of 641.8 eV and 645.3 eV for Mn $2p_3/_2$ and 652.8 eV and 654.1 eV for Mn $2p_1/_2$. These peaks are attributed to the Mn^{2+} and Mn^{4+} oxidation states [112]. In the Mn 2p spectra of the MS/MnIS40 heterostructure (Figure 3.6b), the Mn $2p_3/_2$ and Mn $2p_1/_2$ peaks are slightly shifted towards lower binding energies. Figure 3.6c shows the In 3d spectra for both $MnIn_2S_4$ and MS/MnIS40, where the binding energies of the In 3d peaks at 445.1 eV (In $3d_5/_2$) and 452.7 eV (In $3d_3/_2$) confirm the +3 oxidation state of In in $MnIn_2S_4$. Compared to pure $MnIn_2S_4$, the In 3d XPS peaks in the MS/MnIS40 heterostructures also shift towards lower binding energies.

The Mo 3d spectrum (Figure 3.6d) exhibits two distinct peaks at 229.7 eV and 232.9 eV, corresponding to the binding energies of Mo $3d_{5/2}$ and Mo $3d_{3/2}$, associated with the 2H phase of MoS_2. These findings confirm that Mo in MoS_2 is in the +4 oxidation state. An additional peak observed at a binding energy of 226.8 eV corresponds to the S 2s state, indicating the interaction between S and Mo. Compared to 2D MoS_2, the characteristic Mo 3d peaks of MS/MnIS40 shift slightly to higher binding energies. Conversely, the Mn 2p and In 3d peaks in $MnIn_2S_4$ shift to lower binding energies upon forming MS/MnIS40 heterostructure, suggesting a strong interaction between 2D MoS_2 and $MnIn_2S_4$ [120]. A shift to lower binding energy indicates an increase in electron cloud density, while a shift to higher binding energy implies a decrease in electron cloud density. Consequently, the binding energy shifts observed in the XPS reveal the direction of electron transfer from 2D MoS_2 to $MnIn_2S_4$ in the MS/MnIS40 heterostructure system [49,121–123].

Figure 3.6e displays the HR S 2p spectra of $MnIn_2S_4$, 2D MoS_2, and MS/MnIS40 heterostructure. The S 2p spectrum displays two distinct peaks at 162.2 eV for S $2p_{3/2}$ and 163.5 eV for S $2p_{1/2}$, corresponding to the binding energies of S^{2-} ions in MoS_2 [124]. The S 2p binding energies of $MnIn_2S_4$ were detected at 161.6 eV for S $2p_{3/2}$ and 162.5 eV for S $2p_{1/2}$, respectively. The small peak at a binding energy of 168.9 eV is attributed to sulfate species formed by the oxidation of sulfur in air [125].

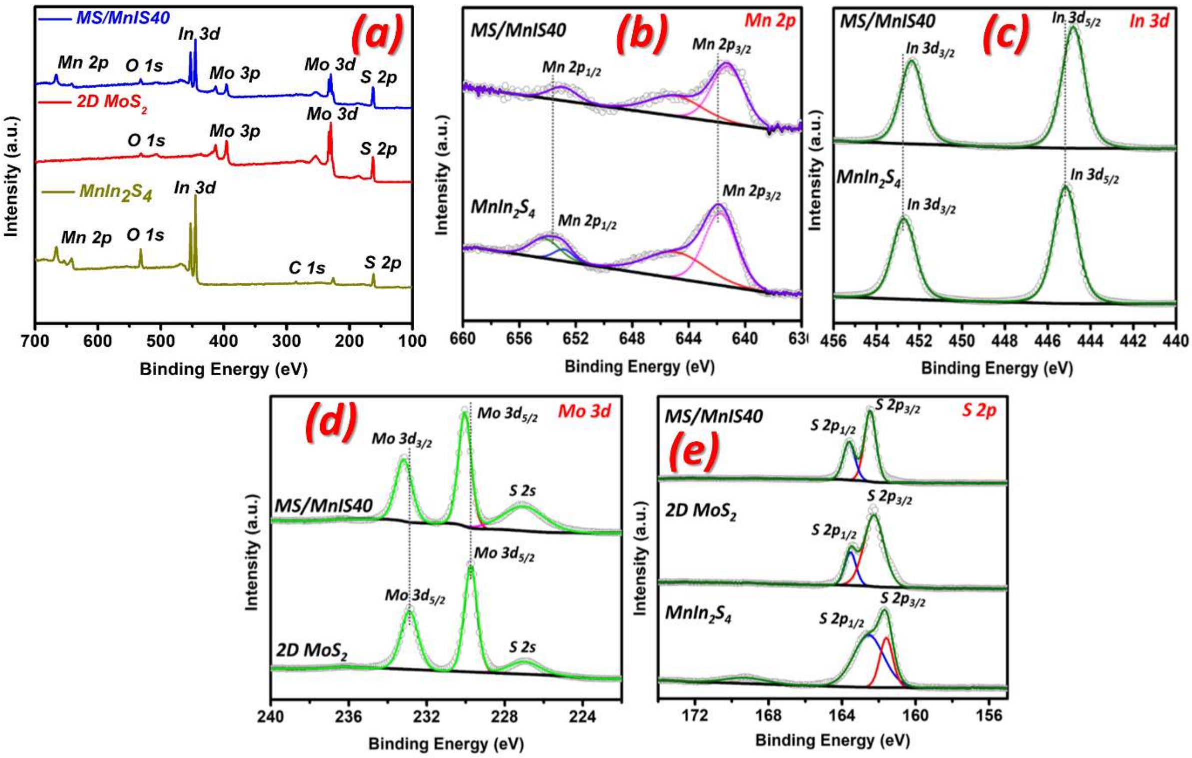

Figure 3.6. (a) XPS spectra of 2D MoS_2, $MnIn_2S_4$, and MS/MnIS40 **(b)** Mn 2p **(c)** In 3d **(d)** Mo 3d **(e)** S 2p.

A photoluminescence (PL) study of the photocatalytic material gives insights into photo-induced charge carriers' migration, transfer, and separation efficiency. Typically, a decrease in the PL emission intensity corresponds to a reduction in the charge carrier recombination rate, indicating enhanced separation of photo-generated electron-hole pairs

[114]. The PL emission spectra of pristine $MnIn_2S_4$ and MS/MnIS-*x*, excited at 340 nm at room temperature, are shown in Figure 3.7a. The PL spectra of MS/MnIS10 and MS/MnIS80 are shown in the Figure 3.7b. A prominent emission peak centered at 450 nm is observed for the as-prepared photocatalysts. In contrast, the MS/MnIS40 heterostructure exhibits the lowest PL intensity among the other photocatalysts. This suggests that loading 40% $MnIn_2S_4$ onto 2D MoS_2 enhances the separation of electron-hole pairs on the catalyst's surface. This enhancement likely contributes to the superior photocatalytic performance of the MS/MnIS40 heterostructure toward the oxygen reduction reaction (ORR). The primary reason is the reduced recombination rate of photo-generated electrons, which allows them to migrate efficiently to the surface of $MnIn_2S_4$, thereby enhancing the photo-reduction process. Furthermore, electrochemical impedance spectroscopy (EIS) was conducted to assess the interfacial charge transfer behavior of the prepared photocatalysts. Figure 3.7c presents the Nyquist plots of the 2D MoS_2 and MS/MnIS-*x* heterostructure systems. Figure 3.7d shows the Nyquist plot of $MnIn_2S_4$, MS/MnIS10, and MS/MnIS80 photocatalysts. As illustrated, the MS/MnIS40 system exhibits the smallest arc diameter, signifying reduced charge transfer resistance and impedance, suggesting improved charge migration [126]. In the MS/MnIS40 heterojunction, the heterostructure formation is well-balanced with a proper interface, ensuring effective electron transport from 2D MoS_2 to $MnIn_2S_4$ while minimizing charge recombination. In contrast, lower $MnIn_2S_4$ loadings (10 wt.% and 20 wt.%) result in insufficient heterojunction formation, leading to higher recombination losses. On the other hand, excessive $MnIn_2S_4$ content (60 wt% and 80 wt%) causes nanosheet agglomeration, which not only covers the active sites on the 2D MoS_2 surface but also leads to charge accumulation, ultimately increasing resistance. Similar results were observed for these materials in the transient photocurrent responses (Figure 3.7e, f). The charge separation process is reflected in the transient photocurrent, as shown by the

chronoamperometry. A significant spike in current occurs immediately upon light exposure, followed by a rapid decline when the light is turned off (Figure 3.7e). Notably, the MS/MnIS40 heterostructure photocatalyst exhibits a significantly higher photocurrent density compared to the other prepared photocatalysts. The photocurrent response of $MnIn_2S_4$, MS/MnIS10, and MS/MnIS80 are given in Figure 3.7f. The combined observations from PL, EIS, and photocurrent experiments demonstrate that the MS/MnIS40 heterostructure can serve as an efficient photocatalyst, exhibiting enhanced photocatalytic H_2O_2 production.

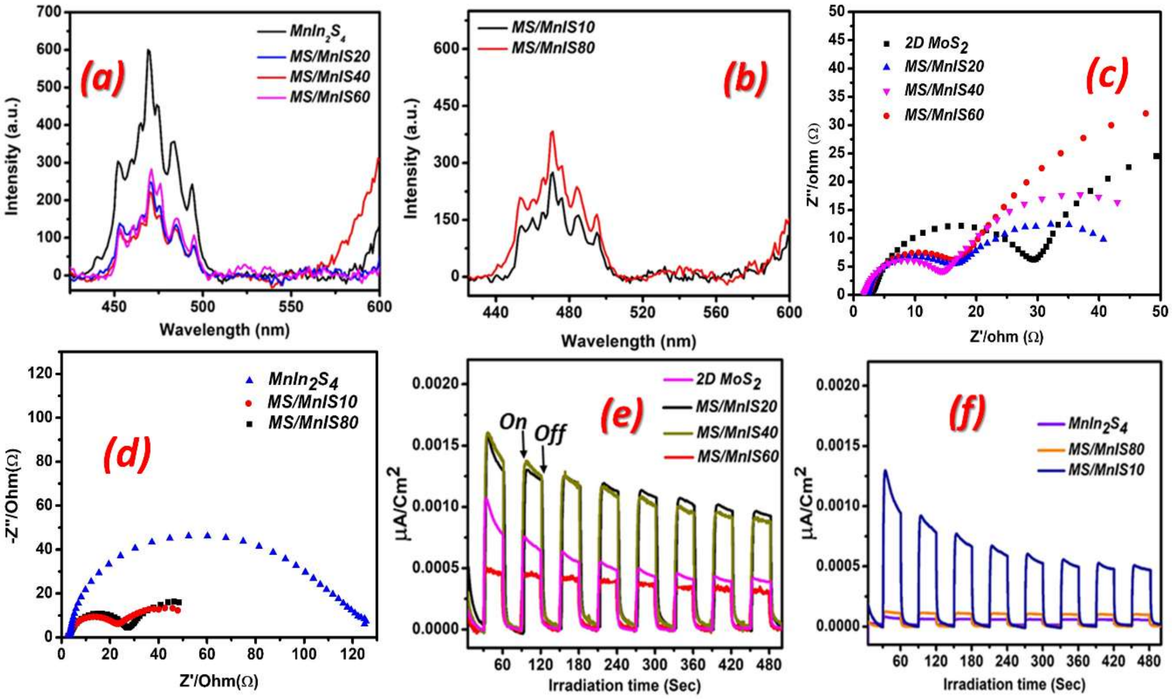

Figure 3.7. (a, b) PL spectra of $MnIn_2S_4$ and MS/MnIS-*x* heterostructure photocatalysts **(c-f)** Nyquist plot and photocurrent studies of 2D MoS_2 and MS/MnIS-*x* heterostructure photocatalysts.

To investigate the impact of photocatalyst surface properties on its activity, contact angle measurements were performed to assess the hydrophilic characteristics of photocatalysts. These experiments were carried out under similar conditions, as a reactant of 5 % (vol) ethanol-containing water was used. After 2 seconds of contact with water/ethanol mixture droplets, the contact angle of 2D MoS_2, $MnIn_2S_4$, MS/MnIS10, MS/MnIS20, MS/MnIS40, MS/MnIS60, and MS/MnIS80 are 43.4°, 14.9°, 37.4°, 30.5°, 23.9°, 20.5 ° and 18.1°; results confirmed its hydrophilic nature (Figure 3.8). A smaller contact angle signifies better wetting of the photocatalyst particle surface by the solvent molecules. It also implies longer residence times for solvent molecules from the water/ethanol mixture, facilitating better contact between the photocatalyst particles and reactants [127]. Additionally, the hydrophilic surface improves the uniform dispersion of the photocatalyst within the reaction system, leading to increased reaction rates and selectivity.

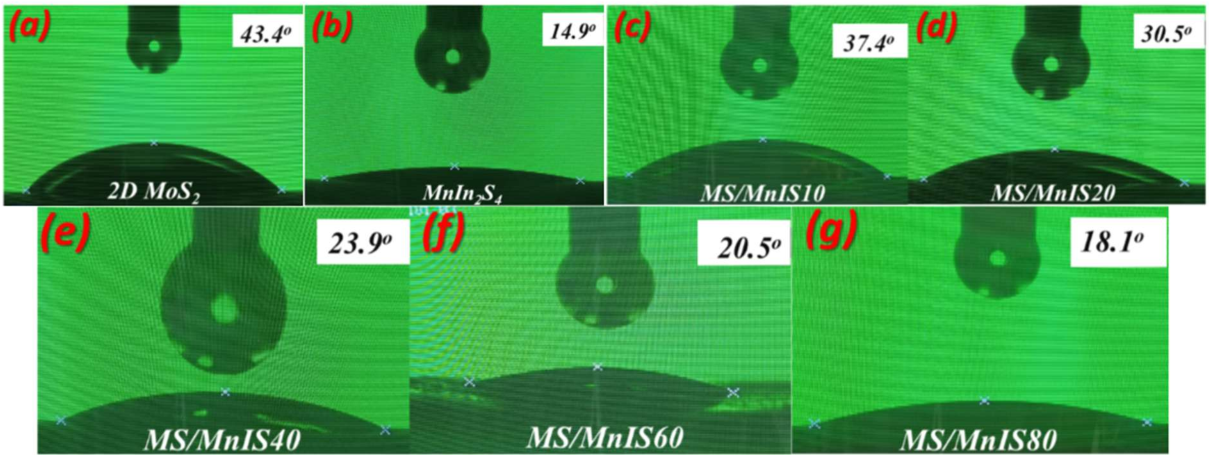

Figure 3.8. Contact angle results **(a)** 2D MoS_2 **(b)** $MnIn_2S_4$ **(c)** MS/MnIS10 **(d)** MS/MnIS20 **(e)** MS/MnIS40 **(f)** MS/MnIS60 **(g)** MS/MnIS80.

3.3.1. Photocatalytic H_2O_2 production

The photocatalytic activities of 2D MoS_2, $MnIn_2S_4$, and MS/MnIS-*x* for H_2O_2 production were evaluated under various controlled conditions at room temperature and atmospheric pressure. Initially, H_2O_2 production was tested without a catalyst or light irradiation. Under these conditions, no H_2O_2 was detected, confirming that the H_2O_2 production reaction at room temperature is driven by solar light in the presence of photocatalysts. Figure 3.9a illustrates the H_2O_2 production rates for different photocatalysts in O_2-bubbled water at pH 3. The MS/MnIS-*x* heterostructure photocatalysts demonstrated significant H_2O_2 formation compared to pristine 2D MoS_2 and $MnIn_2S_4$. Among the various $MnIn_2S_4$ loadings, the 40 wt% loading onto 2D MoS_2 achieved an appreciable H_2O_2 production rate of 240.2 μmol $g^{-1}h^{-1}$. However, further increasing the $MnIn_2S_4$ loading onto the 2D MoS_2 resulted in a decline in H_2O_2 production, likely due to excessive 2D MoS_2 active surface coverage. Moreover, the excess loading caused agglomeration of the nanosheets, as confirmed by the SEM image and elemental mapping of MS/MnIS60 and MS/MnIS80. This excessive coverage impairs visible light absorption and hinders efficient interfacial charge transfer, as evidenced by the EIS and PL results.

In contrast, when ethanol was introduced into the reaction mixture as a sacrificial agent, the photocatalytic H_2O_2 production rate was improved, as shown in Figure 3.9a. Figure 3.9b displays the time-dependent curve of photocatalytic H_2O_2 production of different photocatalysts. This enhancement confirms the oxidation of ethanol by the photogenerated holes. The best-performing photocatalyst, MS/MnIS40, achieved an impressive H_2O_2 production rate of 606.7 μmol g^{-1} h^{-1}, whereas pristine 2D MoS_2 and $MnIn_2S_4$ exhibited only 147.4 μmol g^{-1} h^{-1} and 121.5 μmol g^{-1} h^{-1}, respectively. This corresponds to an approximately 4.2-fold increase compared to pristine 2D MoS_2 and a 5-fold increase compared to $MnIn_2S_4$ alone. Notably, the H_2O_2 generation rate of our MS/MnIS40 surpassed that of recently reported heterostructure-based photocatalysts (Figure 3.9i and Table 3.1).

The photocatalytic H_2O_2 production activity of the best catalyst (MS/MnIS40) was further evaluated at different pH levels (1.5, 3, 5, and 7). The pH-dependent experiments showed that the activity followed the trend: pH 3 > pH 1.5 > pH 5 > pH 7. At pH 3, a significantly enhanced H_2O_2 production rate of 606.7 μmol $g^{-1}h^{-1}$ was achieved (Figure 3.9c), suggesting that protonation-induced ionic species contribute to the improved activity [128]. At a low pH of 1.5, the solution provides an excess of protons (H^+) in the reaction medium, which promotes the oxidation of H_2O_2 to water ($H_2O_2 + 2H^+ + 2e^- \rightarrow 2H_2O$), thereby reducing the overall H_2O_2 yield. Conversely, at pH 5 and 7, the lower availability of protons in the solution results in decreased H_2O_2 formation. Moreover, at a higher pH solution, $\bullet O_2^-$ becomes unstable, and H_2O_2 breaks down more quickly, further lowering its production. Hence, pH 3 was identified as the optimum pH for H_2O_2 production [86,129,130].

To investigate the effect of the heterostructure in MS/MnIS40, control experiments using a physical blend of 60% 2D MoS_2 and 40% $MnIn_2S_4$ photocatalyst were conducted under optimal H_2O_2 production conditions (Figure 3.9d). Under these conditions, the H_2O_2 production rate was only 188.4 μmol g^{-1} h^{-1}, approximately 3.3 times lower than the best photocatalyst (MS/MnIS40). These results confirm that the proper formation of the heterostructure enhances visible light absorption and suppresses charge carrier recombination, leading to higher photocatalytic activity.

To gain further insight into the photocatalytic oxygen reduction reaction (ORR) pathway for H_2O_2 production by the MS/MnIS40 photocatalyst, control experiments with various scavengers were conducted. The photocatalytic performance of MS/MnIS40 was also evaluated under argon (Ar) atmosphere. When the reaction systems were purged with Ar, the H_2O_2 concentration dropped by 82%, demonstrating that O_2 plays a crucial role in the photocatalytic process, with H_2O_2 predominantly formed via the ORR. Interestingly, 18% of the H_2O_2 concentration was retained even under the Ar atmosphere, suggesting that the ORR process subsequently consumes the O_2 generated from water oxidation to produce H_2O_2 (Figure 3.9d). Two potential routes have been reported for synthesizing H_2O_2 from O_2 via a $2e^-$ redox process: a two-step ORR process involving $^{\bullet}O_2^-$ as an intermediate species and a direct $2e^-$ ORR process. To clarify the exact pathway, a $^{\bullet}O_2^-$ scavenger test was conducted using p-BQ. As shown in Figure 3.9e, the scavenger experiment with p-BQ indicated the formation of $\bullet O_2^-$ during the photocatalytic H_2O_2 production pathway, as adding p-BQ reduced H_2O_2 production by 65%. This result confirms that O_2 is reduced to form H_2O_2 through the $^{\bullet}O_2^-$ intermediate via a two-step process [131]. Further validation of $\bullet O_2^-$ involvement was conducted using the NBT test. As shown in Figure 3.9h, NBT is selectively reduced by $\bullet O_2^-$, forming formazan. This reduction is evidenced by decreased NBT absorption intensity with prolonged illumination. The detailed experimental protocol of NBT experiments is provided in Chapter 2. Furthermore, adding $AgNO_3$ confirmed that photo-generated electrons play a crucial role in the photocatalytic process, significantly reducing H_2O_2 production. Similarly, introducing EDTA-2Na as a hole (h^+) scavenger resulted in approximately a 76% reduction in H_2O_2 production compared to the case of no scavenger, highlighting the involvement of h^+ in the photocatalytic reaction. This result suggests that $\bullet O_2^-$ radicals, e^-, and h^+ play a major role in photocatalytic H_2O_2 production (Figure 3.9e).

The photostability of photocatalytic materials is a critical factor influencing H_2O_2 production efficiency. To evaluate this, the recyclability of the MS/MnIS40 photocatalyst for H_2O_2 production was tested over five cycles under identical experimental conditions. After each cycle, the photocatalyst was recovered by centrifugation, rinsed with ethanol, and dried at 60°C for five hours to assess its reusability. The dried photocatalyst was then reused in subsequent cycles. Figure 3.9f illustrates the H_2O_2 production activity of the MS/MnIS40 photocatalyst over five reuse cycles. After five cycles, the MS/MnIS40 heterostructure demonstrated remarkable stability, with H_2O_2 production remaining nearly unchanged and only a slight 7.8% decrease in H_2O_2 formation efficiency. This indicates that the heterostructure maintains its photocatalytic activity well, which is crucial for practical applications. Moreover, we performed XRD and XPS measurements of the recycled photocatalyst, as shown in Figure 3.9g and Figure 3.10. The XRD patterns and XPS spectra of MS/MnIS40 before and after the fifth cycle of the photocatalytic reaction show no noticeable changes, indicating that the crystal structure and chemical states remained stable throughout the recycling process. These findings strongly confirm that the MS/MnIS40 heterostructure exhibits excellent photochemical stability and reusability, which is advantageous for long-term use and continuous operation in photocatalytic H_2O_2 production systems.

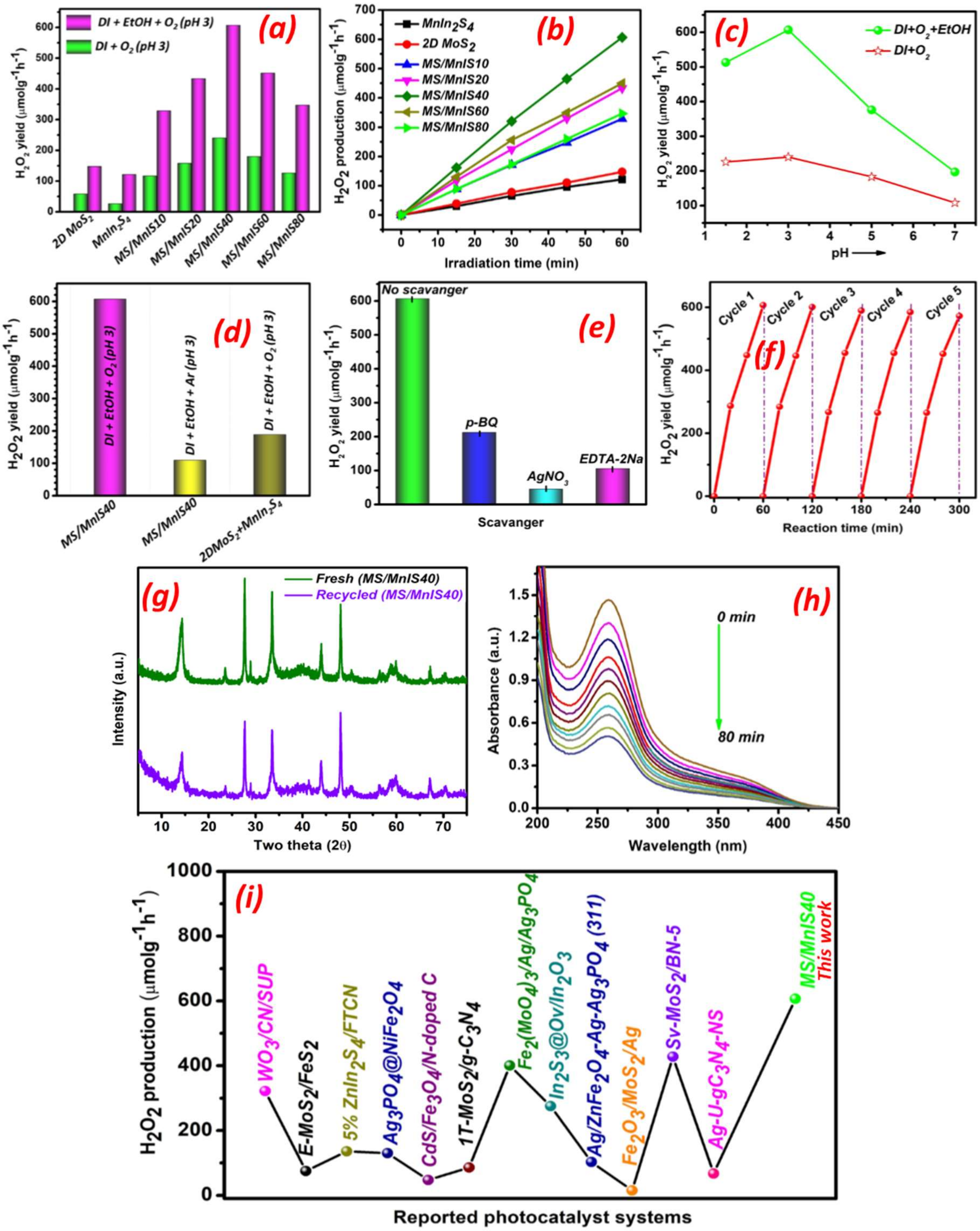

Figure 3.9. (a) H_2O_2 production rates for different photocatalysts in O_2-bubbled water at pH 3. **(b)** The time-dependent plot of photocatalytic H_2O_2 production for various photocatalysts in this chapter. **(c)** H_2O_2 production at different pH levels using the optimal photocatalyst, MS/MnIS40. **(d)** H_2O_2 production under control conditions with

MS/MnIS40. **(e)** H_2O_2 production with MS/MnIS40 in scavenger experiments. **(f)** Cycling experiments showing H_2O_2 production at different time intervals using MS/MnIS40. **(g)** XRD patterns of fresh and recycled MS/MnIS40 photocatalysts **(h)**, NBT experiment on MS/MnIS40 **(i)**, Comparison of photocatalytic H_2O_2 production with recently reported photocatalysts.

Table 3.1. Comparison of photocatalytic H_2O_2 production among recently reported other photocatalytic systems.

Catalysts	Reaction solution	Atmosphere	Light source	H_2O_2 Yield (µmol/g/h)	Ref.
WO_3/CN-SUP	EtOH/Water	O_2	AM 1.5G	322	[132]
E-MoS_2/FeS_2	Water	Air	Visible light	75	[70]
$ZnIn_2S_4$/FTCN50	EtOH/Water	O_2	Visible light	135.98	[133]
Ag_3PO_4@$NiFe_2O_4$	MeOH/Water	O_2	Visible light	130	[64]
CdS/Fe_3O_4/N-doped C	Water	--	Visible light	47.28	[134]
1T-MoS_2/g-C_3N_4	Water	Air	Visible light	86	[135]
$Cu_2(OH)PO_4$/g-C_3N_4	Water	O_2	Simulate solar light	400	[136]
In_2S_3@Ov/In_2O_3	Water	Air	Visible light	275.4	[137]
Ag/$ZnFe_2O_4$-Ag-Ag_3PO_4(111)	EtOH/Water	Air	AM 1.5G filter	103.15	[138]
Fe_2O_3/MoS_2@Ag	Water	--	Visible light	15	[139]
Sv-MoS_2/BN-5	Water	Air	λ > 420 nm	428.17	[140]

$Fe_2(MoO_4)_3/Ag/Ag_3PO_4$	MeOH/Water	--	UV/Visible light	400.8	[141]
Ag@U-g-C_3N_4-NS	Water	--	Visible light	67.50	[142]
MS/MnIS40	Water/EtOH	O_2	Solar Simulator	606.7	This work

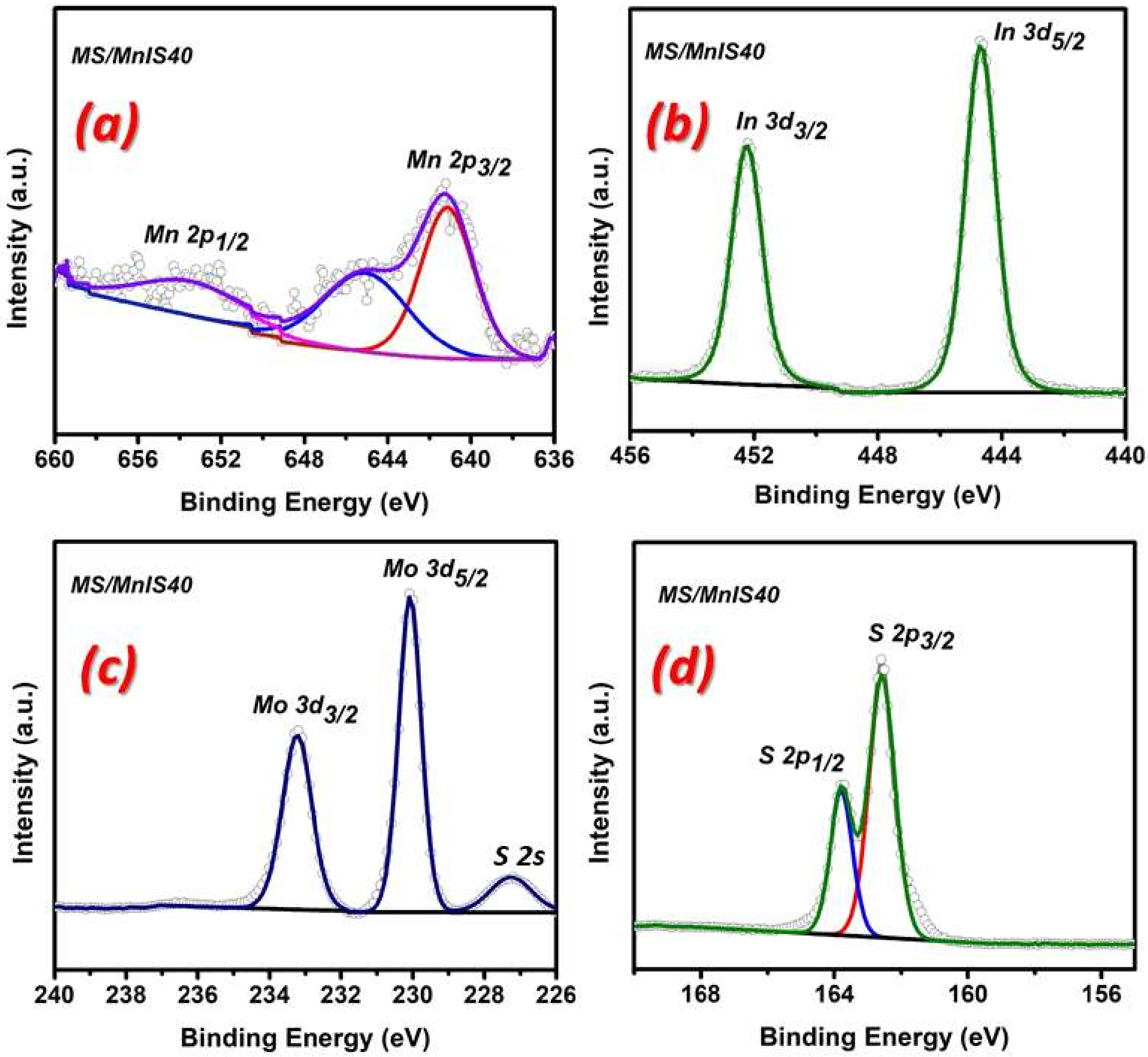

Figure 3.10. XPS spectra of recycled MS/MnIS40 photocatalyst **(a)** Mn 2p, **(b)** In 3d, **(c)** Mo 3d, **(d)** S 2p.

3.4 Photocatalytic Mechanism

The photocatalytic H_2O_2 production of as-prepared photocatalysts performance is presented in Figure 3.9 (a, b). Among them, MS/MnIS40 exhibits the highest photocatalytic activity compared to the other catalysts. Based on the experimental data, a photocatalytic H_2O_2 production mechanism is proposed, as illustrated in Figure 3.11. The combination of 2D MoS_2 and $MnIn_2S_4$ likely forms a Z-scheme heterojunction, as suggested by the Mott-Schottky and scavenger tests. Upon light irradiation of the MS/MnIS40 photocatalyst, photogenerated electrons accumulate in the CB of $MnIn_2S_4$, which has a more negative E_{CB} potential at −0.81 eV (vs. V NHE), closely aligning with the reduction potential of O_2 at −0.33 eV (vs. V NHE). The negative potential of $MnIn_2S_4$ CB and the $O_2/{\bullet}O_2^-$ couple facilitates rapid electron transfer, promoting the two-step one electron O_2 reduction necessary for H_2O_2 generation (Equations 3.2 and 3.3). The significant reduction in H_2O_2 yield in the presence of p-BQ and NBT experiments confirms that ${\bullet}O_2^-$ is the primary active species. This suggests that H_2O_2 is produced through the further conversion of ${\bullet}O_2^-$ radicals, generated by the reduction of O_2 at −0.33 eV (vs. V NHE). Simultaneously, the photo-generated holes in the VB of 2D MoS_2 oxidize water molecules, producing O_2 and H^+ (Equation 3.4), as the VB potential of 2D MoS_2 (+1.42 V vs. NHE) is more positive than the H_2O/O_2 potential (+1.23 V vs. NHE). Control experiments under 'Ar' purging showed that 18% of the H_2O_2 concentration was retained even in the absence of external O_2, suggesting that O_2 is generated from water oxidation. Moreover, the addition of ethanol significantly enhances H_2O_2 production by facilitating its activation, as photo-generated holes are efficiently consumed in the oxidation of ethanol. This reaction also provides H^+ ions, which later react with ${\bullet}O_2^-$ to form H_2O_2 (Equation 3.5) [143]. These factors are crucial for optimizing the photocatalytic ORR process to boost H_2O_2 production.

$O_2 + e^- \rightarrow \cdot O_2^-$………………………………………(3.2)

$\cdot O_2^- + e^- + 2H^+ \rightarrow H_2O_2$…….............................(3.3)

$$2H_2O + 2h^+ \rightarrow O_2 + 2H^+ + 2e^- \text{ ....(3.4)}$$

$$CH_3CH_2OH + 2h^+ \rightarrow CH_3CHO + 2H^+ \text{................(3.5)}$$

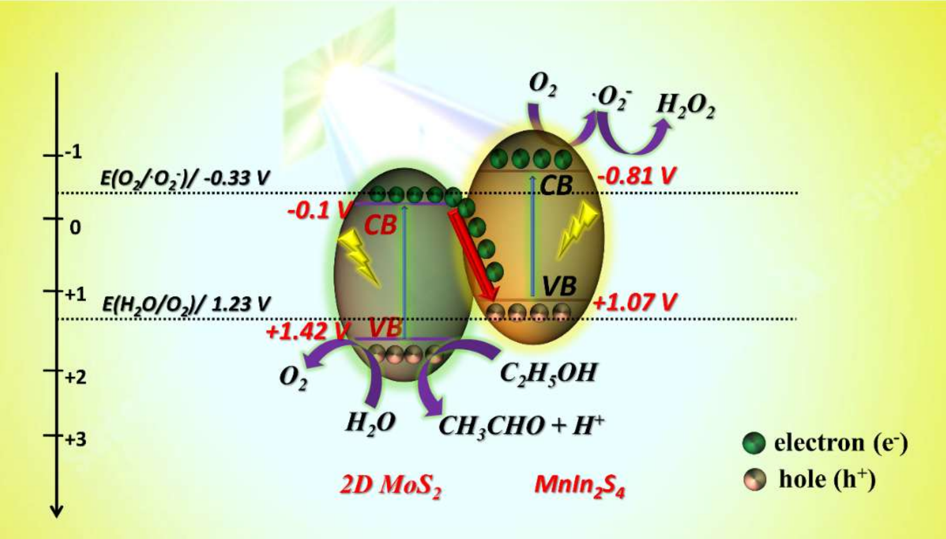

Figure 3.11 Possible mechanism of the photocatalytic H_2O_2 generation on 2D MoS_2/ $MnIn_2S_4$ photocatalyst.

3.5 Conclusions

In conclusion, composite photocatalysts with $MnIn_2S_4$ nanostructures embedded on ultrathin 2D MoS_2 nanosheets have been fabricated for solar-driven H_2O_2 production using a facile two-step hydrothermal method. It was observed that the optimal loading of $MnIn_2S_4$ partially covers the 2D MoS_2 nanosheets, enhancing light absorption and providing more active sites. This leads to improved charge carrier separation and accelerated electron transfer, resulting in enhanced photocatalytic H_2O_2 production. However, excessive loading of $MnIn_2S_4$ covers the surface-active sites of MoS_2 and blocks light absorption, leading to poor interfacial charge carrier separation and reduced photocatalytic activity. Moreover, the poor H_2O_2 production activity observed in physical blending experiments (2D MoS_2 + $MnIn_2S_4$) confirms that when proper heterostructures are formed, the MS/MnIS40 photocatalyst exhibits excellent H_2O_2 production activity, approximately 3.3 times higher than that of the physically blended mixtures. This demonstrates that the formation of an intimately connected/contacted heterostructure effectively inhibits charge recombination and accelerates charge transfer. The microscopy characterization results reveal a strong interfacial interaction between the components of 2D MoS_2 and $MnIn_2S_4$. The controlled radical trapping studies confirmed that H_2O_2 generation preferably occurred via a dual-step, one-electron O_2 reduction pathway. This study can inspire the exploration and development of effective noble-metal-free semiconductor heterostructure photocatalysts for solar-driven H_2O_2 generation.